Nanoscale

PAPER

View Article Online
View Journal | View Issue

Cite this: *Nanoscale*, 2025, **17**, 18190

Heterostructure interface-engineered 3D/2D $CoMn_2O_4/CoFe_2O_4$/NF core/shell Bi-functional electrocatalytic nanomaterials for efficient overall water splitting application in alkaline media†

Moorthy Krishnamachari,[a,b] Mohanraj Kumar,[a,c] Muthu Senthil Pandian[d] and Jih-Hsing Chang *[a]

Developing a high-performance, affordable, reinforced, and stable bi-functional nanocatalyst for a sustainable energy conversion process is highly desirable for large-scale commercialization. Inspired by the benefits of heterostructure engineering, herein, we hierarchically constructed an interface-engineered 3D/2D ($CoMn_2O_4/CoFe_2O_4$) core/shell bi-functional nanohybrid material on a nickel foam (NF) substrate *via* a facile two-step solvothermal process. As evidenced by HR-TEM and XPS results, heterostructure interfaces were properly established, and strong electronic coupling was built at the heterostructure interfaces. Moreover, electrochemical studies revealed that the synergistic coupling effect expedites rapid charge transfer at the electrode/electrolyte interfaces, elevating accessible metal active sites and oxygen vacancies over the nanomaterial surface, and affords robust electrochemical stability to an electrode material. This combined effect greatly elevates electrochemical performance and facilitates remarkably low overpotential values of 104 mV and 233 mV and minimal Tafel slope values of 73.6 mV dec^{-1} and 53.2 mV dec^{-1} for the HER and OER, respectively. Moreover, an assembled two-electrode electrochemical cell setup exhibited a small cell voltage of 1.55 V with stupendous stability over 50 h at a current density of 10 mA cm^{-2} in 1 M KOH alkaline media. This rational core/shell heterostructure interface-constructed bi-functional electrode will be a new avenue for scaling up the electrochemical reaction kinetics of new-generation energy-conversion technologies.

Received 31st March 2025,
Accepted 3rd July 2025

DOI: 10.1039/d5nr01307k

rsc.li/nanoscale

1. Introduction

Extreme dwindling of fossil fuels, elevating energy scarcity and global warming alarm us to switch the pathway to sustainable energy conversion technologies.[1,2] Owing to its high calorific value and long-term sustainable energy supply characteristics, hydrogen (H_2) is considered an ideal candidate compared with other fuel resources.[3,4] Electrochemical water splitting (EWS) is a potent and attractive approach that has been widely employed over recent decades to harvest renewable, ultrapure, nontoxic, and eco-friendly H_2 from naturally abundant water resources.[5,6] Nonetheless, its sluggish and complex 4-stage oxygen evolution reaction (OER) at the anode and 2-stage hydrogen evolution reaction (HER) at the cathode increase the overpotential and hinder its overall commercial applications.[7,8] Presently, Pt-, Ir-, and Ru-doped nanomaterials furnish excellent EWS performances.[9,10] However, the high cost of these metals hampers the industrial-scale production of H_2. Therefore, over the past few decades, massive efforts have been devoted by researchers to construct non-precious, bi-functional electrocatalytic materials. Lately, first-row transition metal complexes such as transition metal oxides,[11] nitrides,[12] sulfides,[13] phosphates,[14] chalcogenides,[15] carbides,[16] and layered double hydroxides[17,18] have been found to exhibit outstanding electrochemical performances owing to their tunable electronic and morphological structures.[19] Particularly, $CoMn_2O_4$ binary transition metal–oxide nanocatalysts have garnered distinct attention owing to their cost-effectiveness, ecological benignity, diverse structural morphologies, multiple oxidation states of Co^+ and Mn^+ ions and rapid redox reaction characteristics.[20–22] Likewise, the distinctive spinel

[a]*Department of Environmental Engineering and Management, Chaoyang University of Technology, Taichung, 413310, Taiwan. E-mail: changjh@cyut.edu.tw; Tel: +886-4-23323000 Ext4210*
[b]*Department of Applied Chemistry, Chaoyang University of Technology, Taichung, 413310, Taiwan*
[c]*Department of Chemistry, Karpagam Academy of Higher Education, Coimbatore, 641021 Tamil Nadu, India*
[d]*SSN Research Centre, Sri Sivasubramaniya Nadar College of Engineering, Kalavakkam, 603110 Tamil Nadu, India*

† Electronic supplementary information (ESI) available. See DOI: https://doi.org/10.1039/d5nr01307k

structure of 2D $CoFe_2O_4$ underlies its notable electrochemical performance owing to its Co ion's larger oxidation potential, larger availability of surface electro-active species with tunable morphology and electronic states furnishing excellent electro catalytic OER property for EWS application.[23,24] Nevertheless, poor electrical conductivity, paucity of active sites and inferior structural stability have been severely limiting the wide-ranging applications of the above-mentioned metal oxides. However, to overcome these shortcomings, several strategies such as doping,[25] alloying,[26] templating,[27] composition modulating,[28] morphological modifications (combination of 1D, 2D, and 3D nanostructures), and heterostructure formation[29–32] have been applied. Amongst them, the heterostructural interface formation is an ingenious strategy that has gained interest in recent times as it triggers spontaneous electron transfer at the interface, increasing metal active sites and oxygen vacancies over the electrode surface, and improves structural and electrochemical stability to the level of electrocatalytic nanomaterials.[32–34] Generally, oxygen vacancies are primary active sites that facilitate optimizing adsorption–desorption binding energies with OER intermediates (OH*, O*, and OOH*) and effectively boost the overall reaction kinetics of electrodes.[35–37] Moreover, the core/shell (3D/2D) structure formation is an another ingenious strategy due to its high surface area, and a 3D core material serves as a scaffold with high surface area for steadily growing 2D ultra-thin nanosheets.[38] This 2D shell-like nanosheet wrapping over the 3D core structure further increases the electrochemical active surface area, which leads to rapid charge transfer for catalytic reactions by shortening the ion diffusion path.[39] Furthermore, the integration of highly efficient hydrogen evolution and oxygen evolution in electrocatalytic materials as a core–shell structure makes them bi-functional electrode materials and enhances the overall system efficiency.[40] Additionally, the shell-like encapsulation provides high stability in a harsh acidic and alkaline medium.[41] In another context, polymer binders (Nafion, polyvinylidene fluoride (PVDF), carboxymethyl cellulose (CMC), *etc.*) greatly elevate the contact resistance at the catalyst/current collector interface, diminishing the metal active sites and declining ion transfer among the electrolyte/electrode surfaces.[42,43] By the way, the solvothermal method is a versatile technique to overcome these limitations and build up binder-free diverse nanoscale dimensions directly on electrically conductive substrates. Moreover, due to its facile, eco-friendliness, energy efficient with controlled nanostructures synthesis declares as an outstanding technique.[44,45]

Lately, several works were initiated to construct effective electrocatalysts for water splitting applications. For example, Junhee Lee *et al.*, demonstrated the synthesis of various single and bimetallic composites of CoO, Mn_2O_3, Co_2MnO_4, and $CoMn_2O_4$ through morphological engineering *via* a solvothermal process. The Density Functional Theory (DFT) calculations clearly demonstrated that the $CoMn_2O_4$ bimetallic spinel structure possesses a lower energy barrier to the dissociation of water molecules to generate H* and deliver excellent HER performance of 132 mV at a current density of 10 mA cm^{-2}.[46] Similarly, *via* a core–shell structural strategy, Iryna Makarchuk and his co-workers constructed Fe_2O_3-magnetite as a core and $CoFe_2O_4$ spinel as a shell by a seed-mediated crystal growth technique. She varied the thickness ratios of the $CoFe_2O_4$ spinel structure and achieved outstanding OER performance at a shell thickness value of 0.65 nm.[47] Moreover, Jiahui Song *et al.* fabricated a $NiO/CoFe_2O_4$ heterostructure *in situ*. Here Ni was used as the low-oxophilic dopant for creating oxygen vacancies. These oxygen vacancies effectively provide optimal adsorption and desorption binding energies for OER intermediates and achieve a low overpotential of 270 mV to deliver a current density of 10 mA cm^{-2} in 1 M KOH.[48]

Inspired by the above-mentioned hypothesis on heterostructure-interfaced nanomaterials, we successfully fabricated binder-free, heterostructure-interfaced, 3D/2D core–shell $CoMn_2O_4/CoFe_2O_4$ bi-functional nanohybrids on conducting NF substrates. This core/shell heterostructured architecture induces a strong and synergistic electronic coupling effect among the $CoMn_2O_4/CoFe_2O_4$ counterpart nanomaterials, which greatly reduces the ion/electron transportation resistance and accelerates the electrochemical reaction. Furthermore, the surface modification process generates numerous active sites, which serve as active centers for the HER and OER intermediates as well as charge storage property. From these advantages of the effective core/shell heterostructure interface strategy, we achieved excellent HER and OER overpotential values of 104 mV and 233 mV and minimal Tafel slope values of 79.9 mV dec^{-1} and 49.5 mV dec^{-1}. Besides, it delivered an outstanding cell voltage of 1.55 V at a current density of 10 mA cm^{-2} in 1 M KOH alkaline media with 50 h robust electrochemical stability.

2. Materials and methods

2.1 Chemicals and reagents

Cobalt nitrate hexahydrate [$Co(NO_3)_2{\cdot}6H_2O$] (99.99%), manganese nitrate tetrahydrate (Mn $(NO_3)_2{\cdot}4H_2O$) (99.99%), iron nitrate nanohydrate [$Fe(NO_3)_3{\cdot}9H_2O$] (99.99%), ammonium fluoride (NH_4F) (99.99%), urea [$CO(NH_2)_2$], ethylene glycol [$(CH_2OH)_2$], DI water, and nickel foam (NF) were used in this experiment.

2.2 Synthesizing procedure

2.2.1 Synthesis of $CoMn_2O_4$ bud-like nanostructures. First, a 3 cm × 2 cm NF substrate was treated with a 3 M concentrated HCl solution *via* a continuous ultrasonification process for 15 min in order to eliminate the surface oxidation layer. Furthermore, it was processed for about 10 min with ethanol and DI water successively. Then, it was dried at 65 °C over 6 h.

The preparation procedure of the $CoMn_2O_4$/NF sample primarily involved that successive addition of 1 mmol of Co $(NO_3)_2{\cdot}6H_2O$, 2 mmol of $Mn(NO_3)_2{\cdot}4H_2O$, 12 mmol of NH_4F, and 24 mmol of $CO(NH_2)_2$, followed by dissolving in 85 mL of distilled water and stirring for 30 min to obtain a homo-

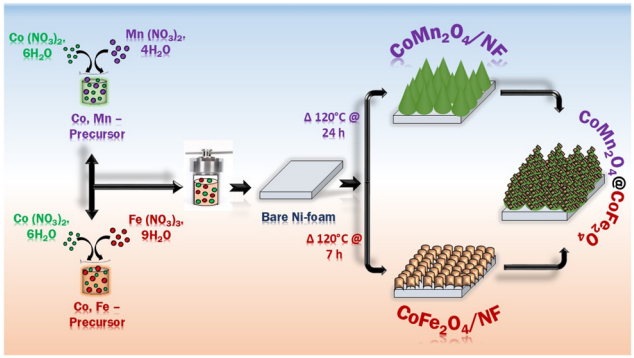

Scheme 1 Schematic of the fabrication procedure of a $CoMn_2O4$/$CoFe_2O_4$ core/shell nanostructure on an Ni-foam substrate.

geneous solution (Scheme 1). The resulting solution was transferred into a 100 mL Teflon autoclave. Then, the cleaned NF substrate was kept in a slanting position in the precursor solution and sealed with a stainless steel covering. The reaction temperature was maintained at 120 °C for 24 h in the furnace. Afterward, it was cooled down to room temperature, and the synthesized CoMo/NF-precursor was cleaned with ethanol and DI water consecutively to remove impurities. Subsequently, the CoMo/NF-precursor was dried at 60 °C for 12 h. Then, the cleaned CoMo/NF-precursor was calcined at 300 °C for 2 h to obtain a $CoMn_2O_4$/NF electrode material.

2.2.2 Synthesis of $CoMn_2O_4$/$CoFe_2O_4$/NF flower bud-like nanostructures. To grow 2D $CoFe_2O_4$ nanosheets over the $CoMn_2O_4$/NF nanobud-like morphology, 40 mL solution of 2 mmol of $Co(NO_3)_2{\cdot}6H_2O$, 4 mmol of $Fe(NO_3)_3{\cdot}9H_2O$, and 24 mmol of $CO(NH_2)_2$ were added to a mixture of ethanol and DI water taken in 1/1 ratio and vigorously stirred for 30 min. Then, the resulting solution was transferred to a 50 mL Teflon autoclave with a slantingly fixed $CoMn_2O_4$/NF substrate. Then, it was maintained in a hot-air oven at 120 °C for 7 h. Later, it was washed with ethanol and DI water sequentially and dried for 6 h. The cleaned substrate was calcined at 400 °C for 2 h to construct a $CoMn_2O_4$/$CoFe_2O_4$/NF flower bud-like morphological heterostructure. Furthermore, for comparison, $CoFe_2O_4$/NF nanosheets were grown over the NF substrate following the above-mentioned procedure, except for the use of a cleaned bar NF substrate instead of $CoMn_2O_4$/$CoFe_2O_4$/NF in the autoclave chamber.

2.3 Physical characterization

The crystalline phases of the prepared electrodes were investigated using a Rigaku Smart Lab X-ray diffractometer (XRD) with Cu-k-alpha radiation (λ = 0.1542 nm). Furthermore, a Thermal Field emission scanning electron microscope (TFE-SEM, Model: JEOL JSM-7800F, 0.01–30 kV, 0.1–1.2 nm resolution) and a high-resolution tunneling electron microscope (HR-TEM, Model: JEOL JEM-2010, 80–200 kV) were used for analyzing the morphological changes of the nanostructures, EDS elemental mapping, crystalline lattice plane, and the SAED pattern of all the fabricated electrode materials. Moreover, the surface ionic states and composition of the synthesized samples were identified using an X-ray photoelectron spectrometer (XPS model: ULVAC-PHI, PHI 5000 Versa Probe, 10 keV, C-60 ion beam).

2.4 Electrochemical measurements

The electrochemical performances of all the synthesized electrodes were measured using a CHI instrument. The typical HER and OER assessment of an electrode was carried out in a N_2-saturated 1 M KOH electrolyte using a three-electrode configuration set-up, in which the synthesized electrodes served as the anode material, a platinum wire as the cathode and a Hg/HgO calomel electrode as the reference electrode. All expressed potentials were relative to the Reversible hydrogen electrode (RHE) following the equation of E(RHE) = E(Hg/HgO) + 0.098 + 0.0591 pH. A scan rate of 5 mV s^{-1} was applied to the analysis of LSV characteristics of all electrodes, and all polarization curves were iR compensated. Furthermore, the general equation is $\eta = b \log I + a$, where η is the over potential value, I is the current density, and b represents the Tafel slope value, which is used for measuring the Tafel slope reaction kinetics. Different scan rates in the range of 20–120 mV s^{-1} were used for the cyclic voltammetry (CV) experiment conducted in the non-faradaic region, and the chemical double layer capacitance (C_{dl}) value was evaluated as $\Delta j = |j_a - j_c|/2$, where, j_a and j_c are the anodic and cathodic current densities. Moreover, the electrochemical active surface area (ESCA) of the electrodes was assessed using the formula ESCA = C_{dl}/C_S, where C_S is the specific capacitance, and the general C_{dl} value was referred from previously reported articles.[49,50] The frequency range of 0.1–100 kHz with an amplitude of 10 mV was provided to investigate the electrochemical impedance spectroscopy (EIS) property. The electrochemical stability of a final composite electrode was assessed by chronoamperometric (i–t) technique at a constant working potential of 1.55 V with a current density of 10 mA cm^{-2}.

3. Results and discussion

3.1 Morphological and electronic structural characterization

The evolution of the nanostructural morphology of the core/shell $CoMn_2O_4$/$CoFe_2O_4$/NF electrocatalyst was investigated by Thermal Field Emission-Scanning Electron Microscope (TFE-SEM) analysis. As depicted in Fig. 1(a–c), the $CoMn_2O_4$ nanocomposite emerged as a 3D bud-like structural morphology, and the alignment of the nanostructure was quite homogeneous with firm anchoring over the NF substrate. Afterwards, the $CoFe_2O_4$ nanocomposite material comprised 2D petals like nanosheets structural morphology, which was corrugated nature with interlinked each other over the NF surface presented at Fig. 1(d–f). More interestingly, after the hierarchical construction of 2D petals such as $CoFe_2O_4$ over the 3D nanobuds such as $CoMn_2O_4$, both were well conjoined with each other and exhibited flower bud-like core/shell $CoMn_2O_4$/$CoFe_2O_4$/NF nano morphological structures, as illus-

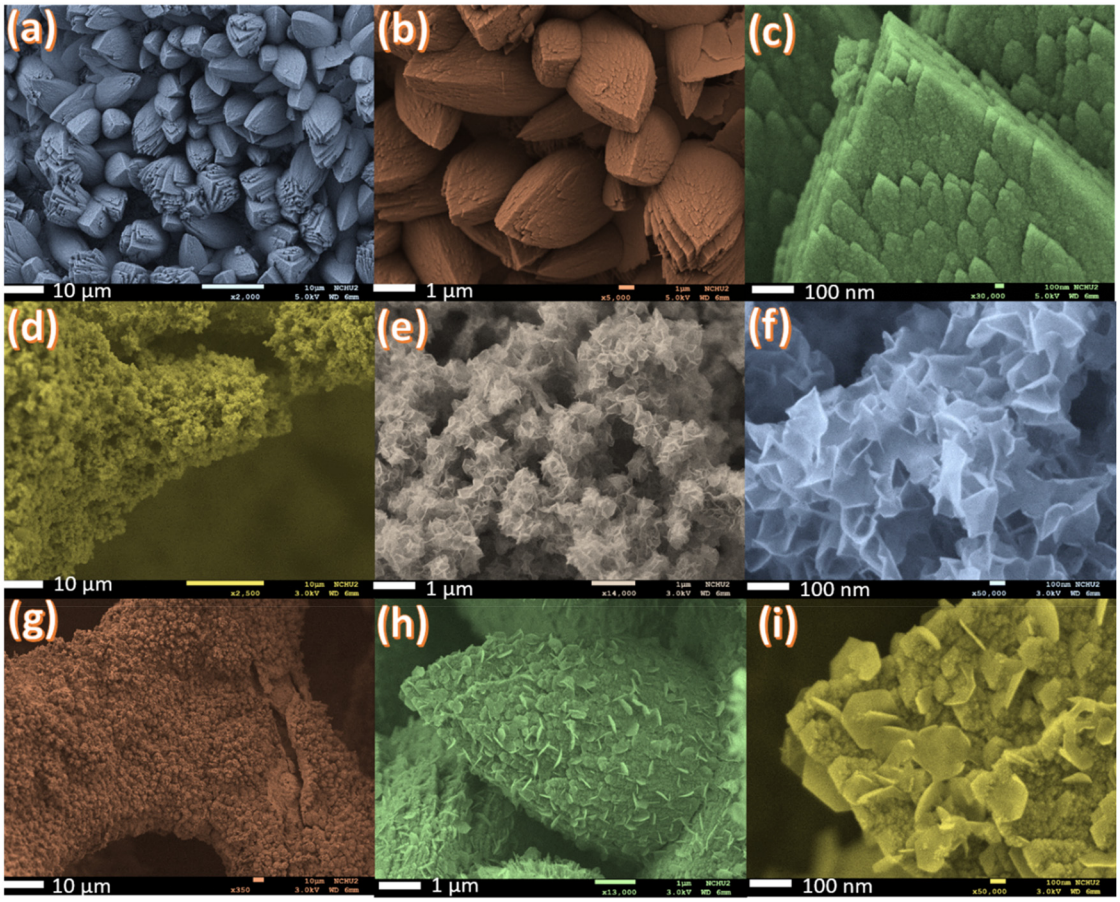

Fig. 1 Low- and high-magnification FE-SEM images of (a–c) $CoMn_2O_4$/NF nanobuds, (d–f) $CoFe_2O_4$/NF nanosheets and (g–i) $CoMn_2O_4$/$CoFe_2O_4$/NF flower bud-like nanomaterials.

trated in Fig. 1(g–i). These heterostructural interface construction enlarges the electrode/electrolyte contact surface area and improves the electrochemical reaction.

Furthermore, the TEM image in Fig. 2a illustrates that the $CoMn_2O_4$/$CoFe_2O_4$ composite material holds a flower bud-like nanomorphological structure, whereas the HR-TEM images displayed in Fig. 2b further display the development of heterostructural interfaces among the $CoMn_2O_4$ and $CoFe_2O_4$ counterpart materials. The marked portions (I, II, III, and IV) were enlarged to indisputably identify the heterostructural interface formation, in which the interplanar spacing values of (0.497 nm), (0.251 nm), (0.303 nm), (0.259 nm), and (0.481 nm) were associated with the crystalline lattice planes of $CoMn_2O_4$ and $CoFe_2O_4$ nanocomposite materials.[51–54] Moreover, the numerous bright spots with diminished rings appeared in the SAED pattern of the $CoMn_2O_4$/$CoFe_2O_4$ composite, as shown in Fig. 2c, which confirmed the slightly polycrystalline nature of the final composite material and the $CoMn_2O_4$ (101), (112), (211) and (224) lattice planes and the $CoFe_2O_4$ (440), (311) and (111) lattice planes, well consistent with the HR-TEM crystalline planes. The Energy-Dispersive X-ray (EDX) spectra with their corresponding elemental mappings are demonstrated in Fig. 2(d and e), which confirmed that all elements were present in the final $CoMn_2O_4$/$CoFe_2O_4$ nanocomposite material.

As disclosed in Fig. 3a, the three dominant peaks at 44.58°, 51.99° and 76.46° in all the synthesized samples apparently affirmed the presence of a metal NF substrate (JCPDS card no. 04–0850). The reflections arising at 18.32°, 29.6°, 33.35°, 36.67°, 58.95°, 61.02°, and 64.93° are well analogous with the (101), (112), (103), (211), (321), (224), and (400) characteristic lattices of the spinal $CoMn_2O_4$ nanostructure (JCPDS card no. 01-077-0471).[55] Similarly, five characteristic peaks at 28.3°, 31.4°, 36.6°, 58.4°, and 63.8° were ascribed to the (2 2 0), (3 1 1), (4 0 0), (5 1 1), and (4 0 0) hexagonal phases of $CoFe_2O_4$ (JCPDS card no. 022-1086).[56] Moreover, all identified peaks with no obvious peaks from other crystalline phases of the $CoMn_2O_4$/$CoFe_2O_4$/NF sample clearly demonstrated that the final core/shell material was constructed with phase purity and well organized. Moreover, it is well united with HR-TEM crystalline lattice planes, which further ensures systemized heterostructural interface formation.

The intrinsic electrocatalytic reactivity of an electrode material was highly associated with the electronic configuration of metal ions, which was analyzed by the XPS technique. The wide-scan survey spectrum in Fig. 3b depicts the presence

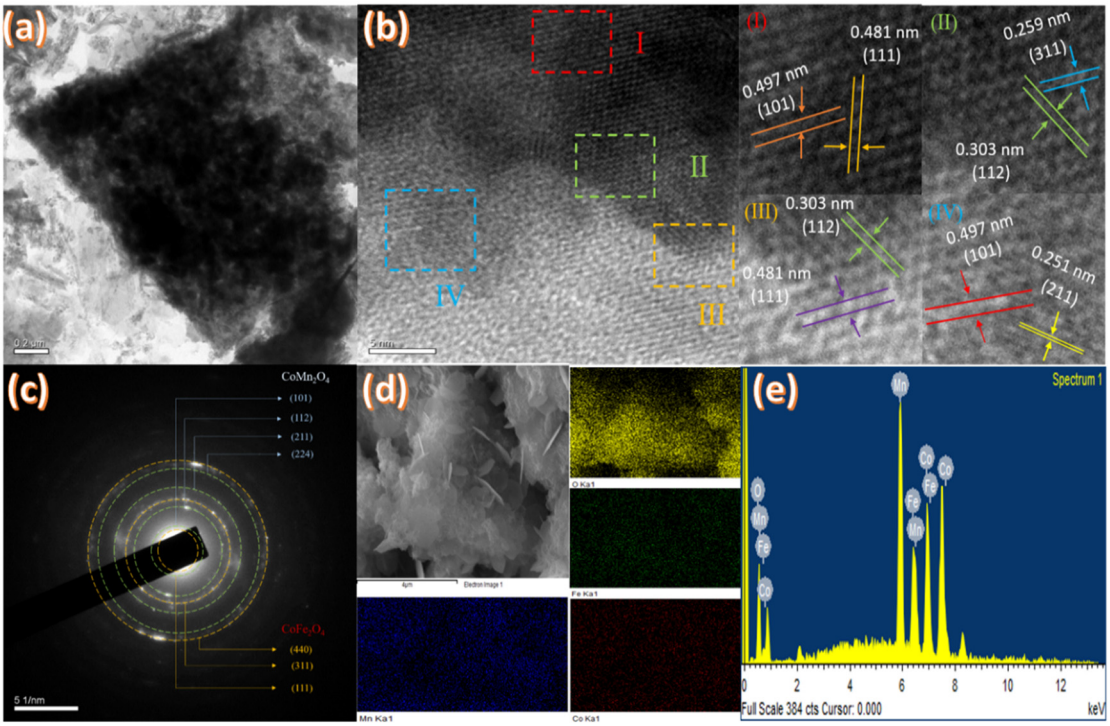

Fig. 2 (a) Low-magnification TEM image. (b) High-resolution TEM lattice planes (1–4 magnified portions). (c) SAED pattern. (d and e) FE-SEM energy-dispersive spectroscopy (EDX) spectra with elemental mappings for the final $CoMn_2O_4/CoFe_2O_4$ nanocomposite.

of elements Co, Mn, Fe, and O in the final cmo/cfo/nf composite material. The electronic configuration of the Co 2p spectra of the $CoMn_2O_4$ nanomaterial shown in Fig. 3c was de-convoluted into two primary oxidation states: Co^{3+} at $2p_{3/2}$ (780.46 eV) and $2p_{1/2}$ (795.95 eV) and Co^{2+} at $2p_{3/2}$ (782.28 eV) and $2p_{1/2}$ (797.06 eV) binding energies with two shakeup satellite peaks (786.30 eV and 802.97 eV),[57,58] whereas the binding energies (638.41 eV)/(650.27 eV) and (640.30 eV)/(651.82 eV) at Fig. 3d should be attributed to the de-convoluted ionic states of (Mn^{3+} and Mn^{2+}) the Mn 2p spectra.[59] As displayed in Fig. 3e, the fitted 4 main peaks at (710.77 eV)/(724.19 eV) and (713.63 eV)/(726.86 eV) binding energies were ascribed to the Fe^{2+} and Fe^{3+} species of the $2p_{3/2}$ and $2p_{1/2}$ spin orbitals along with two satellite shake-up peaks at 715.22 eV and 734.75 eV.[60,61] Furthermore, the O 1s spectrum embraced 3 peaks at 529.83 eV, 531.09 eV, and 533.2 eV in Fig. 3f, which were related to the formation of the Metal–Oxygen bond (O–M*), Oxygen vacancies (O_{vac}), and surface-adsorbed water molecules (O_c).[62] The changes in binding energy at heterogeneous interfaces greatly influence the charge transport property as well as metal active centers during the electrocatalytic reaction.[63–65] Analogously, in our case, after hierarchical nanomorphological reconstruction of $CoFe_2O_4$ nanosheets grown over a pristine $CoMn_2O_4$ nanobud structure, numerous heterostructure interfaces were formed as mentioned by HRTEM and XPS analysis, which effectively modulated the electronic configuration of the final $CoMn_2O_4/CoFe_2O_4$/NF composite material. Essentially, binding energy levels of Co and Mn ions shifted positively towards higher levels by 0.36 eV and 0.41 eV.[66,67] Simultaneously, for Fe ions, it shifted negatively to lower levels by 0.63 eV. These positive and negative binding energy shifts clearly confirmed that strong electronic coupling developed amongst $CoMn_2O_4/CoFe_2O_4$ counterparts. Furthermore, the heterostructure formation created an electric field at the heterostructure interfaces and induced rapid charge transfer from the electron-abundant ($CoMn_2O_4$) composite to the e^- inadequate ($CoFe_2O_4$) material,[68] which may promote the expeditious charge transfer characteristics during the electrochemical reaction. Additionally, electron paramagnetic resonance (EPR) spectroscopy was performed to confirm the presence of oxygen vacancies in each individual material. The $CoMn_2O_4/CoFe_2O_4$ core/shell composite exhibited a significantly higher concentration of oxygen vacancies than the individual components, as depicted in Fig. S1.† This enhancement arises because the formation of the $CoFe_2O_4$ shell onto the $CoMn_2O_4$ core induces interfacial strain and strong electronic coupling. These effects weaken the metal–oxygen bonds near the interface, facilitating oxygen loss and increasing surface oxygen vacancies.[69–71] These increasing oxygen vacancies were employed as an active center for OER intermediates (OH*, O*, and OOH*).

3.2 Electrochemical investigation

Charge transfer characteristics of the fabricated electrodes were investigated by the Electrochemical Impedance spectroscopy (EIS) technique, as displayed in Fig. 4a. Minimal

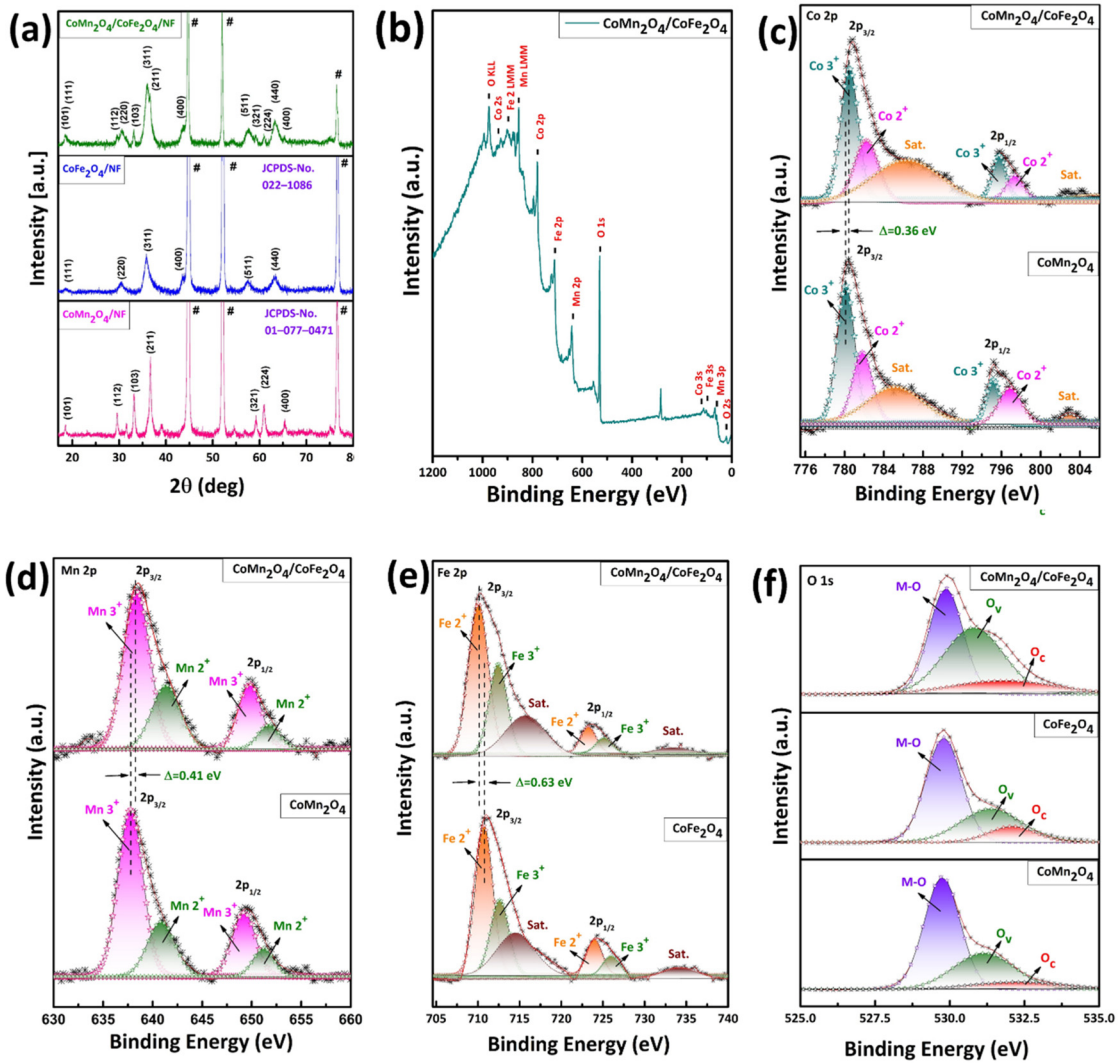

Fig. 3 (a) XRD-patterns. (b) XPS survey and corresponding (c) Co 2p, (d) Mn 2p, (e) Fe 2p, and (f) O 1s spectra of $CoMn_2O_4$, $CoFe_2O_4$, and $CoMn_2O_4$/$CoFe_2O_4$ nanocomposite materials.

charge transfer resistance (R_{ct}) specifies rapid charge transfer at the electrode/electrolyte interface. The Nyquist plots were interpreted in conjunction with the corresponding equivalent electrical circuit model. The lowest R_{ct} value of 118 Ω was obtained for the final core/shell $CoMn_2O_4$/$CoFe_2O_4$/NF heterostructure material compared to the bar NF substrate (283 Ω) and other two nanostructures, $CoMn_2O_4$/NF (139 Ω), $CoFe_2O_4$/NF (147 Ω), respectively. The formation of heterostructural interfaces built an electric field among the counterpart nanocomposites and shortened the charge transfer pathway for rapid charge transfer characteristics to the electrocatalytic reaction.

The electrochemical active surface area (ESCA) is a crucial factor that demonstrates the number of active sites involved in the electrochemical reaction and is also directly proportional to the chemical double-layer capacitance (C_{dl}) of the electrode material. Cyclic voltammetry (CV) is a comfiest and immense technique performed in the non-faradaic region at different scan rates of 20–120 mV s^{-1}, as shown in Fig. S2† to estimate the C_{dl} values of the synthesized electrode materials. The obtained C_{dl} values are depicted in Fig. 4b: for the bar NF substrate, it was 1.08 mF cm^{-2}, and for $CoMn_2O_4$/NF, $CoFe_2O_4$/NF, and $CoMn_2O_4$/$CoFe_2O_4$/NF nanostructures, they were 9.9 mF cm^{-2}, 3.6 mF cm^{-2}, and 17.4 mF cm^{-2}, respectively. As illustrated in the histogram in Fig. 4c, the heterostructured $CoMn_2O_4$/$CoFe_2O_4$/NF nanocomposite entails more active sites of 435 cm^{-2} than the other $CoMn_2O_4$/NF (247 cm^{-2}) and $CoFe_2O_4$/NF (90 cm^{-2}) nanostructured samples, and the bar NF substrate (27 cm^{-2}). The altered morphology and redistributed charge at the heterostructure interfaces lead to increased oxygen vacancies as well as diverse metal active sites across the electrode surface, which act as a major active site for HER as well as OER process.

3.2.1 Electrocatalytic HER performance. Electrocatalytic performance of the synthesized samples was characterized by a linear sweep voltammetry technique in a N_2-saturated 1 M

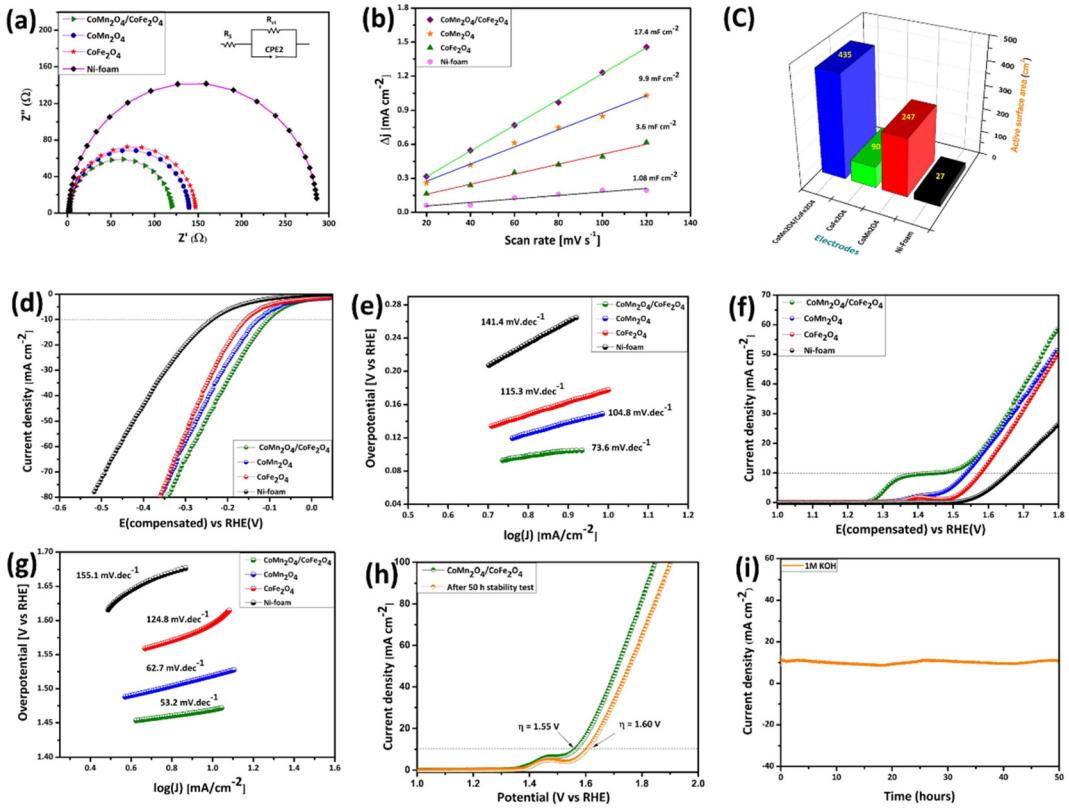

Fig. 4 (a) EIS-Nyquist plots. (b) C_{dl} (Δj *vs.* scan rate) graph. (c) ESCA. (d) LSV-HER. (e) Tafel-HER. (f) LSV-OER. (g) Tafel-OER for all the synthesized electrode materials. (h) LSV-two electrode cell and (i) chronoamperometry (i–t) graph for the final $CoMn_2O_4/CoFe_2O_4$/NF electrocatalytic material.

KOH electrolyte solution at a scan rate of 5 mV s^{-1}. A series of LSV polarization curves for different nanostructures are illustrated in Fig. 4d. Initially, the HER for the bar NF substrate was unsatisfactory, resulting in a larger overpotential value of 235 mV. On the contrary, for $CoMn_2O_4$/NF and $CoFe_2O_4$/NF nanostructured materials, a discernible augmentation of HER activity can be noticed, at 127 mV and 155 mV, respectively, due to the specific morphological structure with moderate electrical conductivity of the counterpart materials. As anticipated, the final core–shell $CoMn_2O_4/CoFe_2O_4$/NF Heterostructured nanohybrid material affords an outstanding performance of 104 mV due to its high ionic conductivity with various metal active sites. To further gain insights into the electrocatalytic mechanism of the electrodes, Tafel slope analysis was performed from LSV polarization cures. Generally, two principal steps are involved in the HER in alkaline media: Volmer-water dissociation step (1) and Heyrovsky (2) or Tafel (3) H_2 evolution process.[72]

$$\text{Volmer}: \ H_2O + e^- \rightarrow H_{ads} + OH^- \quad (1)$$

$$\text{Heyrovsky}: \ H_2O + H_{ads} + e^- \rightarrow H_2 + OH^- \quad (2)$$

$$\text{Tafel}: \ H_{ads} + H_{ads} \rightarrow H_2 \quad (3)$$

In particular, the Volmer water dissociation is a more sluggish and energy-consuming reaction step under alkaline conditions owing to its deficiency of active sites for the H–OH bond severing and H* adsorption as well as the lack of electron transfer characteristics of an electrode material. In our case, the bar NF substrate exhibits a larger slope value of 141.4 mV dec^{-1}. Besides, $CoMn_2O_4$/NF and $CoFe_2O_4$/NF nanostructures over the NF substrate delivered moderate slope values of 115.3 mV dec^{-1} and 104.8 mV dec^{-1}, respectively, which clearly elucidated that the Volmer step is a rate-determining step.[73] As shown in Fig. 4e, the final $CoMn_2O_4/CoFe_2O_4$/NF electrocatalytic material delivered a very minimal slope value of 73.6 mV dec^{-1}, apparently attesting that the construction of core/shell heterostructure interfaces enormously accelerated the HER kinetics of the electrode material. Furthermore, (Mn^{2+}) ions on the $CoMn_2O_4/CoFe_2O_4$/NF electrode surface, additionally serve as a H* adsorption active sites.[74] Moreover, synergistic coupling effects among the pristine $CoMn_2O_4$ and $CoFe_2O_4$ materials facilitate rapid (H*, OH^-*) ion transfer among the electrode/electrolyte interfaces, which further accelerated the HER kinetics.

3.2.2 Electrocatalytic OER performance. Simultaneously, the electrochemical OER performance of the as-prepared electrodes was examined under similar conditions of 1 M KOH electrolyte *via* the LSV polarization technique. Fig. 4f depicts the typical anodic polarization curve of all the fabricated samples, in which the core–shell heterostructured $CoMn_2O_4/CoFe_2O_4$/NF nanohybrid yields a low overpotential value of

231 mV compared to other counterparts, namely bar NF substrate (419 mV), $CoMn_2O_4$/NF (273 mV) and $CoFe_2O_4$/NF (338 mV). In order to investigate the OER kinetics of the electrode materials, Tafel analysis was performed. The fabricated electrocatalytic materials and their corresponding slope values were NF (155.1 mV dec^{-1}), $CoMn_2O_4$/NF (124.8 mV dec^{-1}), $CoFe_2O_4$/NF (62.7 mV dec^{-1}), and $CoMn_2O_4/CoFe_2O_4$/NF (53.2 mV dec^{-1}), respectively. The minimal slope value of the final composite material elucidates that the construction of the core/shell $CoMn_2O_4/CoFe_2O_4$/NF heterostructure interfaces immensely amplifies the OER kinetics, as displayed in Fig. 4g. As mentioned in the XPS data, the surface reconstruction process generates more oxygen defects over the electrode surface and serves as active sites for oxygen reaction intermediates (OH*, O*, and OOH*) during the OER activity.[75,76]

3.2.3 Overall water splitting performance. Encouraged by the fascinating electrocatalytic HER and OER activity of the synthesized electrocatalytic materials, it was assembled as a cathode and anode simultaneously in the electrocatalytic cell (1 M KOH electrolyte), as demonstrated in Fig. 4h, to assess the overall water splitting (OWS) performance of each electrode material, in which the performance of $CoMn_2O_4$ gradually declined over time, whereas $CoFe_2O_4$ demonstrated excellent stability without any noticeable degradation over a period of 50 hours, as shown in Fig. S3.† Interestingly, after the formation of a core/shell heterostructure between these two promising materials, the encapsulation of $CoMn_2O_4$ with sheet-like $CoFe_2O_4$ shells effectively suppressed the structural degradation of $CoMn_2O_4$. This is attributed to the strong electronic coupling between the core and shell components, which enhances the overall structural integrity of the core/shell $CoMn_2O_4/CoFe_2O_4$/NF heterostructured nano-hybrid composite. Moreover, the electrolyte cell only requires 1.55 V at a current density of 10 mA cm^{-2}, and also delivers continuous and stupendous electrochemical stability over 50 h, maintained at the constant current density of 10 mA cm^{-2}, as demonstrated in Fig. 4i.

After the chronoamperometry stability test, the structural stability of the $CoMn_2O_4/CoFe_2O_4$/NF electrocatalysts was inspected using the FE-SEM images shown in Fig. S4(a and b)† and the TEM image shown in Fig. S5.† From these results, it can be understood that the formation of strong heterostructural interfaces among the core/shell nanostructure prohibited morphological deformation. Furthermore, the LSV characteristics shown in Fig. 4h represent that the cell voltage increases by only 1.60 V after 50 h of continuous electrochemical stability. More impressively, the electrochemical performance of the core/shell $CoMn_2O_4/CoFe_2O_4$/NF heterostructured nanomaterial surpasses that of many recently reported bifunctional metal oxide composites (Table ST1†).

Eventually, the superior electrochemical energy conversion characteristics of our present work arise from several morphological and electronic structural modifications. (1) Morphological modification of the construction of a shell (2D $CoFe_2O_4$ nano sheets) over the core (3D $CoMn_2O_4$/NF nanobud)-like structure generously increases the specific surface area of the overall electrode material, which leads to the amplification of huge ion/electron transfer at the electrode–electrolyte interface. This numerous ion/electron transfer enhances H_2 and O_2 evolution. (2) As explained in the XPS technique, strong electronic coupling between two functional materials ($CoMn_2O_4$/$CoFe_2O_4$) builds an electric field at the heterostructural interfaces, which serves as a pathway for rapid electron transfer from the inner core ($CoMn_2O_4$/NF) to the shell ($CoFe_2O_4$) structure and supplies more electrons to the electrochemical HER and OER kinetics. (3) Moreover, these structural and electronic modifications primarily alter the binding energy levels and increase the Co^{3+} ion concentrations and oxygen vacancies over the surface of an electrode material. These species, along with the remaining Fe and Mn metal ions on the electrode surface, serve as active sites for the HER and OER intermediates. (4) The strong electronic coupling among the core and shell materials, together with substrate support, provides firm anchoring and ensures excellent structural and chemical stability in the final $CoMn_2O_4/CoFe_2O_4$/NF core–shell architecture.

4. Conclusion

In summary, a novel, free-standing, homogeneous $CoMn_2O_4$/$CoFe_2O_4$ heterostructure interface-assisted core–shell bi-functional electrocatalytic nanomaterial has been developed on a conducting bar NF substrate *via* a facile two-step solvothermal synthesis route. Through this rational core/shell heterostructure interface construction strategy, the $CoMn_2O_4$/$CoFe_2O_4$/NF nanohybrid demonstrated excellent HER and OER overpotential values of 104 mV and 233 mV and small Tafel slope values of 73.6 mV dec^{-1} and 53.2 mV dec^{-1}. Furthermore, it delivered a remarkable cell voltage of 1.55 V with 50 h of stupendous stability at a constant current density of 10 mA cm^{-2} in 1 M KOH alkaline media. This high-performance $CoMn_2O_4/CoFe_2O_4$/NF heterostructure interface-engineered bi-functional electrocatalyst will be a beneficial contestant for new-generation energy conversion gadgets.

Conflicts of interest

There are no conflicts to declare.

Data availability

Data will be available upon reasonable request.

Acknowledgements

The authors of Chaoyang University of Technology thank the National Science and Technology Council of Taiwan for supporting this work (Grant No.: MOST 111-2221-E-324-004-MY3). We thank the Instrument Center of National Chung Hsing

University for help with FESEM, HRTEM, ESCA, and EPR measurements.

References

1 K. Jiang, Y. Men, R. Xing, B. Fu, G. Shen, B. Li and S. Tao, Divergent Energy-Climate Nexus in the Global Fuel Combustion Processes, *Environ. Sci. Technol.*, 2023, **57**(6), 2506–2515, DOI: **10.1021/acs.est.2c08958**.

2 J. Ren and D. Zhao, Recent Advances in Reticular Chemistry for Clean Energy, Global Warming, and Water Shortage Solutions, *Adv. Funct. Mater.*, 2024, **34**(43), 2307778, DOI: **10.1002/adfm.202307778**.

3 W. Lubitz and W. Tumas, Hydrogen: An Overview, *Chem. Rev.*, 2007, **107**(10), 3900–3903, DOI: **10.1021/cr050200z**.

4 A. Mehtab, S. A. Ali, I. Sadiq, S. Shaheen, H. Khan, M. Fazil, N. A. Pandit, F. Naaz and T. Ahmad, Hydrogen Energy as Sustainable Energy Resource for Carbon-Neutrality Realization, *ACS Sustainable Resour. Manage.*, 2024, **1**(4), 604–620, DOI: **10.1021/acssusresmgt.4c00039**.

5 M. A. Alkhadra, X. Su, M. E. Suss, H. Tian, E. N. Guyes, A. N. Shocron, K. M. Conforti, J. P. de Souza, N. Kim, M. Tedesco, K. Khoiruddin, I. G. Wenten, J. G. Santiago, T. A. Hatton and M. Z. Bazant, Electrochemical Methods for Water Purification, Ion Separations, and Energy Conversion, *Chem. Rev.*, 2022, **122**(16), 13547–13635, DOI: **10.1021/acs.chemrev.1c00396**.

6 M. Itagi, D. Chauhan and Y.-H. Ahn, Wastewater Utilization as a Source for Green Energy Generation Using Alkaline Water Splitting, *ACS EST Water*, 2024, **4**(8), 3550–3557, DOI: **10.1021/acsestwater.4c00424**.

7 A. Raveendran, M. Chandran and R. Dhanusuraman, A Comprehensive Review on the Electrochemical Parameters and Recent Material Development of Electrochemical Water Splitting Electrocatalysts, *RSC Adv.*, 2023, **13**(6), 3843–3876, DOI: **10.1039/D2RA07642J**.

8 A. P. Murthy, J. Theerthagiri and J. Madhavan, Insights on Tafel Constant in the Analysis of Hydrogen Evolution Reaction, *J. Phys. Chem. C*, 2018, **122**(42), 23943–23949, DOI: **10.1021/acs.jpcc.8b07763**.

9 H. Xu, Y. Zhao, G. He and H. Chen, Race on Engineering Noble Metal Single-Atom Electrocatalysts for Water Splitting, *Int. J. Hydrogen Energy*, 2022, **47**(31), 14257–14279, DOI: **10.1016/j.ijhydene.2022.02.152**.

10 M. Iqbal, Y. Bando, Z. Sun, ,K.C.-W. Wu, A. E. Rowan, J. Na, B. Y. Guan and Y. Yamauchi, In Search of Excellence: Convex versus Concave Noble Metal Nanostructures for Electrocatalytic Applications, *Adv. Mater.*, 2021, **33 (13)**, 2004554, DOI: **10.1002/adma.202004554**.

11 S. A. Beknalkar, A. M. Teli and J. C. Shin, Current Innovations and Future Prospects of Metal Oxide Electrospun Materials for Supercapacitor Technology: A Review, *J. Mater. Sci. Technol.*, 2023, **166**, 208–233, DOI: **10.1016/j.jmst.2023.04.066**.

12 M. Batool, A. Hameed and M. A. Nadeem, Recent Developments on Iron and Nickel-Based Transition Metal Nitrides for Overall Water Splitting: A Critical Review, *Coord. Chem. Rev.*, 2023, **480**, 215029, DOI: **10.1016/j.ccr.2023.215029**.

13 M. Wang, L. Zhang, Y. He and H. Zhu, Recent Advances in Transition-Metal-Sulfide-Based Bifunctional Electrocatalysts for Overall Water Splitting, *J. Mater. Chem. A*, 2021, **9**(9), 5320–5363, DOI: **10.1039/D0TA12152E**.

14 Y. Zhang, J. Wu, B. Guo, H. Huo, S. Niu, S. Li and P. Xu, Recent Advances of Transition-Metal Metaphosphates for Efficient Electrocatalytic Water Splitting, *Carbon Energy*, 2023, **5**(12), e375, DOI: **10.1002/cey2.375**.

15 K. C. Majhi and M. Yadav, Transition Metal-Based Chalcogenides as Electrocatalysts for Overall Water Splitting, *ACS Eng. Au*, 2023, **3**(5), 278–284, DOI: **10.1021/acsengineeringau.3c00014**.

16 M. S. Arif Sher Shah, G. Y. Jang, K. Zhang and J. Park, H. mTransition Metal Carbide-Based Nanostructures for Electrochemical Hydrogen and Oxygen Evolution Reactions, *EcoEnergy*, 2023, **1**(2), 344–374, DOI: **10.1002/ece2.18**.

17 D. P. Sahoo, K. K. Das, S. Mansingh, S. Sultana and K. Parida, Recent Progress in First Row Transition Metal Layered Double Hydroxide (LDH) Based Electrocatalysts towards Water Splitting: A Review with Insights on Synthesis, *Coord. Chem. Rev.*, 2022, **469**, 214666, DOI: **10.1016/j.ccr.2022.214666**.

18 P. Vijayakumar, S. Lenus, K. Pradeeswari, M. Kumar, J.-H. Chang, M. Kandasamy, M. Krishnamachari, Z. Dai, A. A. Al-Kahtani and P. S. Krishnan, In Situ Reconstructed Layered Double Hydroxides via MOF Engineering and Ru Doping for Decoupled Acidic Water Oxidation Enhancement, *Energy Fuels*, 2024, **38**(5), 4504–4515, DOI: **10.1021/acs.energyfuels.3c04641**.

19 M. N. Lakhan, A. Hanan, A. Hussain, I. A. Soomro, Y. Wang, M. Ahmed, U. Aftab, H. Sun and H. Arandiyan, Transition Metal-Based Electrocatalysts for Alkaline Overall Water Splitting: Advancements, Challenges, and Perspectives, *Chem. Commun.*, 2024, **60**(39), 5104–5135, DOI: **10.1039/D3CC06015B**.

20 J. Vigneshwaran, A. Sakthivel, A. Kumari, R. L. Narayan, V. Chakkravarthy, D. Ghosh and S. P. Jose, Efficiently Designed Three-Dimensional Architecture of CoMn2O4 Decorated V2CTx MXene for Asymmetric Supercapacitors, *ACS Appl. Mater. Interfaces*, 2024, **16**(49), 67553–67566, DOI: **10.1021/acsami.4c09937**.

21 A. Bahadur, W. Hussain, S. Iqbal, F. Ullah, M. Shoaib, G. Liu and K. Feng, A Morphology Controlled Surface Sulfurized CoMn2O4 Microspike Electrocatalyst for Water Splitting with Excellent OER Rate for Binder-Free Electrocatalytic Oxygen Evolution, *J. Mater. Chem. A*, 2021, **9**(20), 12255–12264, DOI: **10.1039/D0TA09430G**.

22 R. Abazari, S. Sanati, A. Morsali and D. P. Dubal, High Specific Capacitance of a 3D-Metal–Organic Framework-Confined Growth in CoMn2O4 Nanostars as Advanced

Supercapacitor Electrode Materials, *J. Mater. Chem. A*, 2021, **9**(17), 11001–11012, DOI: 10.1039/D1TA00900A.

23 D. Gogoi, M. R. Das and N. N. Ghosh, CoFe2O4 Hollow Spheres-Decorated Three-Dimensional rGO Sponge for Highly Efficient Electrochemical Charge Storage Devices, *ACS Omega*, 2022, **7**(13), 11305–11319, DOI: 10.1021/acsomega.2c00374.

24 H. Zhang, G. Qian, X. Chen, W. Jiang, T. Yu, Y. Wang, L. Luo and S. Yin, V2O3-Decorated Spinel CoFe2O4 with Carbon-Encapsulated Mesoporous Nanosheets for Efficient Water Splitting, *ACS Sustainable Chem. Eng.*, 2021, **9**(2), 980–986, DOI: 10.1021/acssuschemeng.0c08477.

25 H. Sun, Y. Min, W. Yang, Y. Lian, L. Lin, K. Feng, Z. Deng, M. Chen, J. Zhong, L. Xu and Y. Peng, Morphological and Electronic Tuning of Ni2P through Iron Doping toward Highly Efficient Water Splitting, *ACS Catal.*, 2019, **9**(10), 8882–8892, DOI: 10.1021/acscatal.9b02264.

26 F. Qin, Z. Zhao, M. K. Alam, Y. Ni, F. Robles-Hernandez, L. Yu, S. Chen, Z. Ren, Z. Wang and J. Bao, Trimetallic NiFeMo for Overall Electrochemical Water Splitting with a Low Cell Voltage, *ACS Energy Lett.*, 2018, **3**(3), 546–554, DOI: 10.1021/acsenergylett.7b01335.

27 S. Park, M. Shviro, H. Hartmann, A. Besmehn, J. Mayer, D. Stolten and M. Carmo, Nickel Structures as a Template Strategy to Create Shaped Iridium Electrocatalysts for Electrochemical Water Splitting, *ACS Appl. Mater. Interfaces*, 2021, **13**(11), 13576–13585, DOI: 10.1021/acsami.0c23026.

28 J. Duan, S. Chen, A. Vasileff and S. Z. Qiao, Anion and Cation Modulation in Metal Compounds for Bifunctional Overall Water Splitting, *ACS Nano*, 2016, **10**(9), 8738–8745, DOI: 10.1021/acsnano.6b04252.

29 M. Qin, L. Chen, H. Zhang, M. Humayun, Y. Fu, X. Xu, X. Xue and C. Wang, Achieving Highly Efficient pH-Universal Hydrogen Evolution by Mott-Schottky Heterojunction of Co2P/Co4N, *Chem. Eng. J.*, 2023, **454**, 140230, DOI: 10.1016/j.cej.2022.140230.

30 B. Chen, M. Humayun, Y. Li, H. Zhang, H. Sun, Y. Wu and C. Wang, Constructing Hierarchical Fluffy CoO–Co4N@NiFe-LDH Nanorod Arrays for Highly Effective Overall Water Splitting and Urea Electrolysis, *ACS Sustainable Chem. Eng.*, 2021, **9**(42), 14180–14192, DOI: 10.1021/acssuschemeng.1c04674.

31 Y. Wang, L. Chen, H. Zhang, M. Humayun, J. Duan, X. Xu, Y. Fu, M. Bououdina and C. Wang, Elaborately Tailored NiCo2O4 for Highly Efficient Overall Water Splitting and Urea Electrolysis, *Green Chem.*, 2023, **25**(20), 8181–8195, DOI: 10.1039/D3GC01828H.

32 M. Krishnamachari, M. Kumar, M. S. Pandian and J.-H. Chang, Hierarchical Construction of 3D Binder-Free NiMoO4/CoFe2O4/NF Arrays to Enhance Water Splitting and Charge-Storage Efficiency, *J. Colloid Interface Sci.*, 2025, **680**, 613–622, DOI: 10.1016/j.jcis.2024.11.117.

33 A. Gaur, J. Sharma and V. Bagchi, Electronic Redistribution Through the Interface: A Prodigy That Enhances Electrocatalysis, *ChemCatChem*, 2024, **16**(4), e202301438, DOI: 10.1002/cctc.202301438.

34 Y. Zhang, P. Chen, Q. Wang, Q. Wang, K. Zhu, K. Ye, G. Wang, D. Cao, J. Yan and Q. Zhang, High-Capacity and Kinetically Accelerated Lithium Storage in MoO3 Enabled by Oxygen Vacancies and Heterostructure, *Adv. Energy Mater.*, 2021, **11**(31), 2101712, DOI: 10.1002/aenm.202101712.

35 W. Li, L. Zhao, C. Wang, X. Lu and W. Chen, Interface Engineering of Heterogeneous CeO_2–CoO Nanofibers with Rich Oxygen Vacancies for Enhanced Electrocatalytic Oxygen Evolution Performance, *ACS Appl. Mater. Interfaces*, 2021, **13**(39), 46998–47009, DOI: 10.1021/acsami.1c11101.

36 Z. Xiao, Y. Wang, Y.-C. Huang, Z. Wei, C.-L. Dong, J. Ma, S. Shen, Y. Li and S. Wang, Filling the Oxygen Vacancies in Co3O4 with Phosphorus: An Ultra-Efficient Electrocatalyst for Overall Water Splitting, *Energy Environ. Sci.*, 2017, **10**(12), 2563–2569, DOI: 10.1039/C7EE01917C.

37 J. Kumar, H. J. Jung, R. R. Neiber, R. A. Soomro, Y. J. Kwon, N. U. Hassan, M. Shon, J. H. Lee, K.-Y. Baek and K. Y. Cho, Recent Advances in Oxygen Deficient Metal Oxides: Opportunities as Supercapacitor Electrodes, *Int. J. Energy Res.*, 2022, **46**(6), 7055–7081, DOI: 10.1002/er.7675.

38 L. Yu, H. Zhou, J. Sun, F. Qin, F. Yu, J. Bao, Y. Yu, S. Chen and Z. Ren, Cu Nanowires Shelled with NiFe Layered Double Hydroxide Nanosheets as Bifunctional Electrocatalysts for Overall Water Splitting, *Energy Environ. Sci.*, 2017, **10**(8), 1820–1827, DOI: 10.1039/C7EE01571B.

39 Q. Yang, Y. Cui, Q. Li, J. Cai, D. Wang and L. Feng, Nanosheet-Derived Ultrafine CoRuOx@NC Nanoparticles with a Core@Shell Structure as Bifunctional Electrocatalysts for Electrochemical Water Splitting with High Current Density or Low Power Input, *ACS Sustainable Chem. Eng.*, 2020, **8**(32), 12089–12099, DOI: 10.1021/acssuschemeng.0c03410.

40 G. Rajeshkhanna, A. Borah, T. I. Singh, T. H. Nguyen, V. A. Dinh, N. H. Kim and J. H. Lee, Counter Ion-Regulated Heterostructured Co@Fe-Based Core@shell Materials: As Remarkable Bifunctional Electrodes for Green H2 Production, *J. Mater. Chem. A*, 2024, **12**(36), 24656–24669, DOI: 10.1039/D4TA02785J.

41 Y. Liu, W. Li, Y. Ma and D. Fan, Core–Shell Dendritic Superstructural Catalysts by Design for Highly Efficient and Stable Electrochemical Oxygen Evolution Reaction, *Adv. Mater. Interfaces*, 2020, **7**(16), 2000777, DOI: 10.1002/admi.202000777.

42 A. Tandon, S. Rani and Y. Sharma, Designing the Binder-Free Conversion-Based Manganese Oxide Nanofibers as Highly Stable and Rate-Capable Anode for Next-Generation Li-Ion Batteries, *ACS Appl. Energy Mater.*, 2022, **5**(6), 6855–6868, DOI: 10.1021/acsaem.2c00487.

43 R. Ma, X. Zhang, J. Zhuo, L. Cao, Y. Song, Y. Yin, X. Wang, G. Yang and F. Yi, Self-Supporting, Binder-Free, and Flexible Ti3C2Tx MXene-Based Supercapacitor Electrode with Improved Electrochemical Performance, *ACS Nano*, 2022, **16**(6), 9713–9727, DOI: 10.1021/acsnano.2c03351.

44 K.MØ. Jensen, C. Tyrsted, M. Bremholm and B. B. Iversen, In Situ Studies of Solvothermal Synthesis of Energy

Materials, *ChemSusChem*, 2014, **7**(6), 1594–1611, DOI: 10.1002/cssc.201301042.

45 S. K. Jain, M. Fazil, N. A. Pandit, S. A. Ali, F. Naaz, H. Khan, A. Mehtab, J. Ahmed and T. Ahmad, Modified, Solvothermally Derived Cr-Doped SnO2 Nanostructures for Enhanced Photocatalytic and Electrochemical Water-Splitting Applications, *ACS Omega*, 2022, **7**(16), 14138–14147, DOI: 10.1021/acsomega.2c00707.

46 J. Lee, N. Son, N.-K. Park, H.-J. Ryu, J.-I. Baek, Y. Sohn, J. Y. Do and M. Kang, Electrochemical Behavior of the Flower Shaped CoMn2O4 Spinel Structure Assembled for Effective HER from Water Splitting, *Electrochim. Acta*, 2021, **379**, 138168, DOI: 10.1016/j.electacta.2021.138168.

47 Effect of Shell Thickness on the Oxygen Evolution Activity of Core@shell Fe3O4@CoFe2O4 Nanoparticles | Chemistry of Materials. https://pubs.acs.org/doi/full/10.1021/acs.chemmater.4c01784 (accessed 2025–06–30).

48 J. Song, W. Ge, S. Deng, Q. Zhou, S. Deng and P. Yang, *In situ* Constructing of NiO/CoFe2O4 Heterojunction through Oxophilicity Engineering for Efficient Water Oxidation, *J. Alloys Compd.*, 2025, **1016**, 178952, DOI: 10.1016/j.jallcom.2025.178952.

49 Q. Sun, Y. Dong, Z. Wang, S. Yin and C. Zhao, Synergistic Nanotubular Copper–Doped Nickel Catalysts for Hydrogen Evolution Reactions, *Small*, 2018, **14**(14), 1704137, DOI: 10.1002/smll.201704137.

50 W. Gao, Y. Shi, Y. Zhang, L. Zuo, H. Lu, Y. Huang, W. Fan and T. Liu, Molybdenum Carbide Anchored on Graphene Nanoribbons as Highly Efficient All-pH Hydrogen Evolution Reaction Electrocatalyst, *ACS Sustainable Chem. Eng.*, 2016, **4**(12), 6313–6321, DOI: 10.1021/acssuschemeng.6b00859.

51 M. Zhou, D. Yoon, Y. Yang, L. Zhang, C. Li, H. Wang, A. Sharma, S. Jiang, D. A. Muller, H. D. Abruña and J. Fang, Enhanced Oxygen Reduction Performance on {101} CoMn2O4 Spinel Facets, *ACS Energy Lett.*, 2023, **8**(8), 3631–3638, DOI: 10.1021/acsenergylett.3c01376.

52 L. Hu, H. Zhong, X. Zheng, Y. Huang, P. Zhang and Q. Chen, CoMn2O4 Spinel Hierarchical Microspheres Assembled with Porous Nanosheets as Stable Anodes for Lithium-Ion Batteries, *Sci. Rep.*, 2012, **2**(1), 986, DOI: 10.1038/srep00986.

53 C. Cannas, A. Ardu, A. Musinu, L. Suber, G. Ciasca, H. Amenitsch and G. Campi, Hierarchical Formation Mechanism of CoFe2O4 Mesoporous Assemblies, *ACS Nano*, 2015, **9**(7), 7277–7286, DOI: 10.1021/acsnano.5b02145.

54 K. Srinivas, Y. Chen, Z. Su, B. Yu, M. Karpuraranjith, F. Ma, X. Wang, W. Zhang and D. Yang, Heterostructural CoFe2O4/CoO Nanoparticles-Embedded Carbon Nanotubes Network for Boosted Overall Water-Splitting Performance, *Electrochim. Acta*, 2022, **404**, 139745, DOI: 10.1016/j.electacta.2021.139745.

55 M. Prabu, P. Ramakrishnan, H. Nara, T. Momma, T. Osaka and S. Shanmugam, Zinc–Air Battery: Understanding the Structure and Morphology Changes of Graphene-Supported CoMn2O4 Bifunctional Catalysts Under Practical Rechargeable Conditions, *ACS Appl. Mater. Interfaces*, 2014, **6**(19), 16545–16555, DOI: 10.1021/am5047476.

56 S. Mitra, P. S. Veluri, A. Chakraborthy and R. K. Petla, Electrochemical Properties of Spinel Cobalt Ferrite Nanoparticles with Sodium Alginate as Interactive Binder, *ChemElectroChem*, 2014, **1 (6)**, 1068–1074, DOI: 10.1002/celc.201400026.

57 J. Béjar, F. Espinosa-Magaña, M. Guerra-Balcázar, J. Ledesma-García, L. Álvarez-Contreras, N. Arjona and L. G. Arriaga, Three-Dimensional-Order Macroporous AB2O4 Spinels (A, B = Co and Mn as Electrodes in Zn–Air Batteries, *ACS Appl. Mater. Interfaces*, 2020, **12**(48), 53760–53773, DOI: 10.1021/acsami.0c14920.

58 M. Harada, F. Kotegawa and M. Kuwa, Structural Changes of Spinel MCo2O4 (M = Mn, Fe, Co, Ni, and Zn Electrocatalysts during the Oxygen Evolution Reaction Investigated by In Situ X-Ray Absorption Spectroscopy, *ACS Appl. Energy Mater.*, 2022, **5**(1), 278–294, DOI: 10.1021/acsaem.1c02824.

59 T. Kokulnathan, V. Rajagopal, T.-J. Wang, S.-J. Huang and F. Ahmed, Electrochemical Behavior of Three-Dimensional Cobalt Manganate with Flowerlike Structures for Effective Roxarsone Sensing, *Inorg. Chem.*, 2021, **60**(23), 17986–17996, DOI: 10.1021/acs.inorgchem.1c02583.

60 T. Saravanakumar, S. Sathiya Bama, T. Selvaraju and S. J. Sardhar Basha, Hexacyanoferrate-Complex-Derived NiFe2O4/CoFe2O4 Heterostructure–MWCNTs for an Efficient Oxygen Evolution Reaction, *Energy Fuels*, 2021, **35**(6), 5372–5382, DOI: 10.1021/acs.energyfuels.0c04224.

61 X. Xu, M. Liu, Y. Nie, C. Wang, W. Wang, C. Liu, X. Wang, Z. Cai, X. Liu, S. Huo, B. Liu and J. Zou, Modulating Electronic Structure of Interfacial Fe Sites in Fe2N/CoFe2O4 Nano-Heterostructure for Enhancing Corrosion-Resistance and Oxygen Electrocatalysis in Zinc-Air Battery, *Chem. Eng. J.*, 2023, **471**, 144639, DOI: 10.1016/j.cej.2023.144639.

62 C. Dong, Z. Qu, Y. Qin, Q. Fu, H. Sun and X. Duan, Revealing the Highly Catalytic Performance of Spinel CoMn2O4 for Toluene Oxidation: Involvement and Replenishment of Oxygen Species Using In Situ Designed-TP Techniques, *ACS Catal.*, 2019, **9**(8), 6698–6710, DOI: 10.1021/acscatal.9b01324.

63 M. Fu, W. Chen, Y. Lei, H. Yu, Y. Lin and M. Terrones, Biomimetic Construction of Ferrite Quantum Dot/Graphene Heterostructure for Enhancing Ion/Charge Transfer in Supercapacitors, *Adv. Mater.*, 2023, **35**(21), 2300940, DOI: 10.1002/adma.202300940.

64 Q. Sun, Y. Li, J. Hao, S. Zheng, T. Zhang, T. Wang, R. Wu, H. Fang and Y. Wang, Increased Active Sites and Charge Transfer in the SnS2/TiO2 Heterostructure for Visible-Light-Assisted NO2 Sensing, *ACS Appl. Mater. Interfaces*, 2021, **13**(45), 54152–54161, DOI: 10.1021/acsami.1c16095.

65 S. Zhao, Y. Yang and Z. Tang, Insight into Structural Evolution, Active Sites, and Stability of Heterogeneous

Electrocatalysts, *Angew. Chem., Int. Ed.*, 2022, **61**(11), e202110186, DOI: **10.1002/anie.202110186**.

66 J. Luo, W. H. Guo, Q. Zhang, X. H. Wang, L. Shen, H. C. Fu, L. L. Wu, X. H. Chen, H. Q. Luo and N. B. Li, One-Pot Synthesis of Mn–Fe Bimetallic Oxide Heterostructures as Bifunctional Electrodes for Efficient Overall Water Splitting, *Nanoscale*, 2020, **12**(38), 19992–20001, DOI: **10.1039/D0NR05864E**.

67 J. Qin, Y. Long, G. Gou, W. Wu, Y. Luo, X. Cao, S. Luo, K. Wang and J. Ma, Tuning Effect of Amorphous Fe2O3 on Mn3O4 for Efficient Atom-Economic Synthesis of Imines at Low Temperature: Improving [O] Transfer Cycle of Mn3+/Mn2 + in Mn3O4, *Catal. Sci. Technol.*, 2020, **10**(16), 5628–5640, DOI: **10.1039/D0CY01021A**.

68 X. Liu, P. Liu, F. Wang, X. Lv, T. Yang, W. Tian, C. Wang, S. Tan and J. Ji, Plasma-Induced Defect Engineering and Cation Refilling of $NiMoO_4$ Parallel Arrays for Overall Water Splitting, *ACS Appl. Mater. Interfaces*, 2021, **13**(35), 41545–41554, DOI: **10.1021/acsami.1c09084**.

69 Comparing the Impacts of Strain Types on Oxygen-Vacancy Formation in a Perovskite Oxide via Nanometer-Scale Strain Fields | ACS Nano. **https://pubs.acs.org/doi/full/10.1021/acsnano.4c03783** (accessed 2025–06–30).

70 Y. Zhang, J. Liu, Y. Xu, C. Xie, S. Wang and X. Yao, Design and Regulation of Defective Electrocatalysts, *Chem. Soc. Rev.*, 2024, **53**(21), 10620–10659, DOI: **10.1039/D4CS00217B**.

71 Advances in Noble Metal Electrocatalysts for Acidic Oxygen Evolution Reaction: Construction of Under–Coordinated Active Sites – Wang – 2024 - Advanced Science - Wiley Online Library. **https://advanced.onlinelibrary.wiley.com/doi/full/10.1002/advs.202401652** (accessed 2025–06–30).

72 S. Watzele, J. Fichtner, B. Garlyyev, J. N. Schwämmlein and A. S. Bandarenka, On the Dominating Mechanism of the Hydrogen Evolution Reaction at Polycrystalline Pt Electrodes in Acidic Media, *ACS Catal.*, 2018, **8**(10), 9456–9462, DOI: **10.1021/acscatal.8b03365**.

73 J. Huang, J. Han, T. Wu, K. Feng, T. Yao, X. Wang, S. Liu, J. Zhong, Z. Zhang, Y. Zhang and B. Song, Boosting Hydrogen Transfer during Volmer Reaction at Oxides/Metal Nanocomposites for Efficient Alkaline Hydrogen Evolution, *ACS Energy Lett.*, 2019, **4**(12), 3002–3010, DOI: **10.1021/acsenergylett.9b02359**.

74 L. Shen, Q. Zhang, J. Luo, H. C. Fu, X. H. Chen, L. L. Wu, H. Q. Luo and N. B. Li, Heteroatoms Adjusting Amorphous FeMn-Based Nanosheets via a Facile Electrodeposition Method for Full Water Splitting, *ACS Sustainable Chem. Eng.*, 2021, **9**(17), 5963–5971, DOI: **10.1021/acssuschemeng.1c00521**.

75 Y. Liu, Y. Hu, X. Zhao, S. Zhu, Y. Min, Q. Xu and Q. Li, Oxygen Vacancy and Heterostructure Modulation of Co2P/Fe2P Electrocatalysts for Improving Total Water Splitting, *ACS Appl. Mater. Interfaces*, 2024, **16**(11), 13795–13805, DOI: **10.1021/acsami.3c19548**.

76 T. Li, L. Zhang, J. Wang, X. Zhang, L. Zhang, M. Wang, C. Yan and T. Qian, Facilitating Reconstruction of the Heterointerface Electronic Structure by the Enriched Oxygen Vacancy for the Oxygen Evolution Reaction, *Inorg. Chem.*, 2023, **62**(26), 10504–10512, DOI: **10.1021/acs.inorgchem.3c01666**.